

NASA/TM—20230009506



Blade Deformation Measurements of the HVAB Rotor in Hover by Stereo Photogrammetry

Edward T. Schairer

James T. Heineck

Michelle Dominguez

Thomas R. Norman

NASA Ames Research Center, Moffett Field, CA 94035-1000

July 2023

NASA STI Program ... in Profile

Since its founding, NASA has been dedicated to the advancement of aeronautics and space science. The NASA scientific and technical information (STI) program plays a key part in helping NASA maintain this important role.

The NASA STI program operates under the auspices of the Agency Chief Information Officer. It collects, organizes, provides for archiving, and disseminates NASA's STI. The NASA STI program provides access to the NTRS Registered and its public interface, the NASA Technical Reports Server, thus providing one of the largest collections of aeronautical and space science STI in the world. Results are published in both non-NASA channels and by NASA in the NASA STI Report Series, which includes the following report types:

- **TECHNICAL PUBLICATION.** Reports of completed research or a major significant phase of research that present the results of NASA Programs and include extensive data or theoretical analysis. Includes compilations of significant scientific and technical data and information deemed to be of continuing reference value. NASA counterpart of peer-reviewed formal professional papers but has less stringent limitations on manuscript length and extent of graphic presentations.
- **TECHNICAL MEMORANDUM.** Scientific and technical findings that are preliminary or of specialized interest, e.g., quick release reports, working papers, and bibliographies that contain minimal annotation. Does not contain extensive analysis.
- **CONTRACTOR REPORT.** Scientific and technical findings by NASA-sponsored contractors and grantees.
- **CONFERENCE PUBLICATION.** Collected papers from scientific and technical conferences, symposia, seminars, or other meetings sponsored or co-sponsored by NASA.
- **SPECIAL PUBLICATION.** Scientific, technical, or historical information from NASA programs, projects, and missions, often concerned with subjects having substantial public interest.
- **TECHNICAL TRANSLATION.** English-language translations of foreign scientific and technical material pertinent to NASA's mission.

Specialized services also include organizing and publishing research results, distributing specialized research announcements and feeds, providing information desk and personal search support, and enabling data exchange services.

For more information about the NASA STI program, see the following:

- Access the NASA STI program home page at <http://www.sti.nasa.gov>
- E-mail your question to help@sti.nasa.gov
- Phone the NASA STI Information Desk at 757-864-9658
- Write to:
NASA STI Information Desk
Mail Stop 148
NASA Langley Research Center
Hampton, VA 23681-2199



Blade Deformation Measurements of the HVAB Rotor in Hover by Stereo Photogrammetry

Edward T. Schairer

James T. Heineck

Michelle Dominguez

Thomas R. Norman

NASA Ames Research Center, Moffett Field, CA 94035-1000

National Aeronautics and
Space Administration

Ames Research Center
Moffett Field, CA 94035-1000

July 2023

Acknowledgments

The authors gratefully acknowledge the support of the entire HVAB test team (NASA, NFAC, and U.S. Army). Special thanks go to test directors Scott Edwards and Paul Gilles.

This report is available in electronic form at <http://>

Abstract

Bending and elastic twist of blades of a four-bladed rotor in hover were measured by stereo photogrammetry as part of the test campaign of the Hover Validation and Acoustic Baseline (HVAB) rotor in the National Full-Scale Aerodynamic Complex at NASA Ames Research Center. The rotor blades were imaged from below by two scientific digital cameras mounted on the floor of the test section 46 feet apart and 40 feet below the rotor plane. Retro-reflective targets were placed in rows of four at 20 radial stations on the lower surface of each blade and were illuminated by flash-lamps co-located with the cameras. Bending and elastic twist were computed by comparing target locations measured at loaded and unloaded conditions after accounting for differences due to rigid-body displacements and rotations. Differences between repeated measurements of bending and elastic twist at ostensibly the same test conditions were larger than expected probably due to unsteady recirculation in the test section. These effects were mitigated by averaging five repeated measurements at each test condition and by averaging measurements of all four blades. The data averaged in this way showed smooth increases in bending and nose-down elastic twist as the collective pitch set point was increased.

Contents

Abstract	3
Nomenclature	6
1. Introduction	7
2. Test facility	8
3. Test article.....	9
3.1 Rotor blades and test stand.....	9
3.2 Targets	10
4. Photogrammetry system	11
4.1 Cameras and lamps	11
4.2 Camera calibration.....	13
4.2.1 Internal orientation	13
4.2.2 External orientation	13
5. Data Acquisition	14
5.1 NFAC Data Acquisition System	14
5.2 Photogrammetry data acquisition.....	15
6. Photogrammetry data reduction.....	15
6.1 Locate targets.....	15
6.2 Compute 3D coordinates	16
6.3 Compute rigid-body transformation	16
6.4 Transform targets to blade coordinates and compute bending and elastic twist	17
6.5 Details on elastic twist and “real-world” issues.....	17
7. Test results	18
7.1 A single test point.....	18
7.2 Repeated test points	19
7.3 Blade-to-blade comparisons	20
7.4 Effects of collective pitch and RPM	21
7.5 Pitch, flap, and lag	22
8. Discussion	22
8.1 Repeatability.....	22
8.1.1 Cycle-to-cycle “jitter”	23
8.1.2 Bending measurement repeatability	24
8.1.3 Elastic twist measurement repeatability	26
8.2 Uncertainty	26
8.2.1 Random errors	27
8.2.2 Bias errors	28
8.2.3 Effect of the number of rigid-body targets	28

8.3 Lessons learned	29
9. Database	29
9.1 Bending and elastic twist	29
9.2 Pitch, flap, and lag	30
10. Concluding remarks	30
11. References	31
12. Appendix	32

Nomenclature

c_x, c_y	scale factors in horizontal and vertical directions, pixels
DZ	bending perpendicular to rotor plane, in
K_1, K_2	correction factors for 1 st - and 2 nd -order symmetrical lens distortion
m_{ij}	elements of 3x3 rotation matrix
M_{tip}	tip Mach number
r	radial distance from hub, in also distance of image point from principal point, pixels
R	radius of rotor = 66.5, in
x	distance south from rotor hub, in (distance south of quarter chord when $\psi = 90^\circ$)
y	distance east from rotor hub, in (along elastic axis of rotor blade at $\psi = 90^\circ$)
z	distance above rotor plane, in
x_c, y_c, x_c	3D coordinates of camera perspective center, in
X, Y	image-plane pixel coordinates after correction for lens distortion = (0, 0) at top-left corner
X_d, Y_d	image-plane pixel coordinates before correction for lens distortion
X_p, Y_p	principal point: pixel coordinates where the optical axis passes through image plane
Θ	collective pitch angle = angle of attack at $r/R = 0.75$ (no elastic twist), deg
Θ_0	collective pitch set point = angle of attack at $r/R = 0.75$ (no elastic twist), deg
β	flap angle: blade rigid-body rotation in the vertical plane about the hinge point, positive for tip higher than root, deg
ζ	lead/lag angle: blade rigid-body rotation in the horizontal plane about the hinge point, positive for tip ahead of root (lead), deg
ψ	azimuth angle: angle in the horizontal plane in true tunnel coordinates (= $0^\circ, 90^\circ, 180^\circ, 270^\circ$ when blade pointed south, east, north, and west, respectively), deg

1. Introduction

Validation of computational methods for predicting the performance of rotors in hover requires an extensive experimental database. In response to this need, an 11.08-ft diameter rotor was tested in hover in the 80- by 120-Ft test section of the National Full-Scale Aerodynamic Complex (NFAC), operated by the Air Force at NASA Ames Research Center. The blade set is known as the Hover Validation and Acoustic Baseline (HVAB)¹. In addition to more conventional measurements of thrust, torque, pitch, flap and lag by instrumentation in the rotor hub, other measurements were made using three optical techniques: infrared thermography to measure transition to turbulence of the boundary layers on the upper and lower surfaces of the rotor blades; retro-reflective shadowgraphy to visualize tip vortices; and stereo photogrammetry to measure blade deformations. An overview of the test and sample data from all measurement techniques was presented at the Vertical Flight Society 79th Annual Forum in 2023². The present report provides a more complete description of the blade deformation measurements and presents data over the full range of test conditions.

Stereo photogrammetry is an optical technique that allows measuring the 3D positions of points in space (“points of interest”) by simultaneously acquiring images of the points from different directions using two or more calibrated cameras. If the points of interest are targets that lie on the surface of a wind-tunnel model, the elastic deformation of the model can be computed by comparing the 3D coordinates of the targets measured at loaded (e.g., “wind-on”) and unloaded (e.g., “wind-off”) test conditions. In the general case, differences in target coordinates between loaded and unloaded conditions will be due to both rigid-body displacement and/or rotation and elastic deformation. To separate these effects, it is necessary to compute a six-degree-of-freedom rigid-body transformation between the loaded and unloaded conditions. This is usually accomplished using a set of targets on the test article that are rigidly connected. After this transformation is applied to all targets, including those on elastic parts of the test article, remaining differences with respect to the unloaded target coordinates are due to model deformation.

Photogrammetry is now widely used to measure deformation of models of fixed-wing aircraft during tests in production wind-tunnels. Brooks and Beamish³ were among the first to make such measurements. They used film cameras and a simplified mapping from 3D object space to the 2D image plane of each camera (Direct Linear Transformation⁴) to measure deformation of an aircraft model in the Langley 8-Ft Transonic Pressure Tunnel. With the advent of high-resolution digital cameras and high-speed computers, model deformation measurements of fixed-wing models by stereo photogrammetry can be made in real time.

Stereo photogrammetry has also been used to measure bending and elastic twist of rotor blades during tests in wind tunnels. Photogrammetry was used to measure blade deformations of a full-scale UH-60A rotor in forward flight in the 40- by 80-Ft test section of the NFAC⁵. Eight floor-mounted digital cameras with wide-angle lenses were required to measure the blades over the full range of azimuths. More recently, photogrammetry was used to measure deformations of the 11.2-ft diameter PSP Rotor in forward flight in the Langley 14- by 22-Ft Subsonic Wind Tunnel⁶. Measurements were made over a range of azimuth angles by two cameras mounted to a turntable in the floor of the test section.

Measuring deformation of a rotor blade introduces several obvious difficulties that are not present in tests of fixed-wing test articles: most notably, points of interest—targets on the blades—are moving at high speed and accelerating inward. The high speed requires very short camera integration times to avoid blurring and also creates high shear stress which, together with centrifugal force, can dislodge adhesive targets. Another difficulty is the absence of a truly rigid surface to which “rigid-body” targets can be applied. This increases the uncertainty in separating loaded vs. unloaded target displacements into rigid- and flexible-body contributions. Further complicating rotor measurements are the typically very high aspect ratio of rotor blades and, for measurements in forward flight, the changing position of the blades at different

azimuths. Thus, the region of interest is typically very large and, to capture it all, it is necessary to use wide-angle lenses (resulting in lower spatial resolution and higher lens distortion) and/or more than two cameras. Together, lens distortion, low spatial resolution, and small chord lengths increase the uncertainties in blade-deformation measurements, especially measurements of elastic twist.

In many ways, the present test was similar to the previous test of the PSP rotor in the Langley 14- by 22-Ft Subsonic Wind Tunnel. Except for a fairing at the blade root, the as-designed outer-mold-lines of the HVAB and PSP blades were identical. Although the lengths of the blades were also the same, the diameter of the PSP rotor was one inch larger than the HVAB rotor due to differences in the hubs. In both tests adhesive retro-reflective targets were applied to the lower surfaces of the rotor blades and were imaged by two cameras below the rotor. The most important difference between the tests was that the PSP rotor was tested in forward flight whereas the HVAB rotor was tested in hover only. This difference greatly simplified the HVAB test since blade deformation measurements were only required at a single azimuth. Another important difference was the scale of the test facility: with both rotors mounted equidistant between the floor and ceiling, the PSP rotor was only seven feet above the floor compared to 40 feet for the HVAB rotor. An important goal of the HVAB test was to measure elastic twist with an uncertainty of 0.1° or less.

This report describes how blade-deformation measurements of the HVAB rotor were made and presents results over the full range of test conditions. It also provides a guide to the blade-deformation portion of the NASA HVAB database.



Figure 1. The National Full-Scale Aerodynamics Complex.

2. Test facility

The tests were conducted in the 80- by 120-Ft test section of the NFAC, which is operated by the Air Force at NASA Ames Research Center (Fig. 1). With its acoustic liner, the test section is 79 feet high by 119 feet wide and approximately 192 feet long. The test section is part of a non-return leg of the facility whereby outside ambient air is drawn through the test section by six 40-ft diameter fans, each driven by a 23,500 hp motor, downstream of the diffuser. Maximum airspeed in the 80- by 120-ft test section is approximately 100 kts. A turning-vane set at the downstream end of the diffuser can be closed when the closed-return 40- by 80-ft test section is in use. For the present hover test the vane set was closed and there was no net flow through

the test section. The test section served as a large hover chamber, open at its upstream end (the inlet), and closed at all other boundaries.

In the absence of flow through the test section, we replace “upstream” and “downstream” with “North” and “South”, respectively. The origin of the tunnel axes was defined as the center of the hub. The longitudinal axis (x) was positive south of the hub and negative north of the hub and passed through $\psi = 0^\circ$ and $\psi = 180^\circ$, respectively. The lateral (y) axis was positive toward the east wall and negative toward the west wall and passed through $\psi = 90^\circ$ and $\psi = 270^\circ$, respectively. The vertical (z) axis was positive toward the ceiling (Fig. 2).

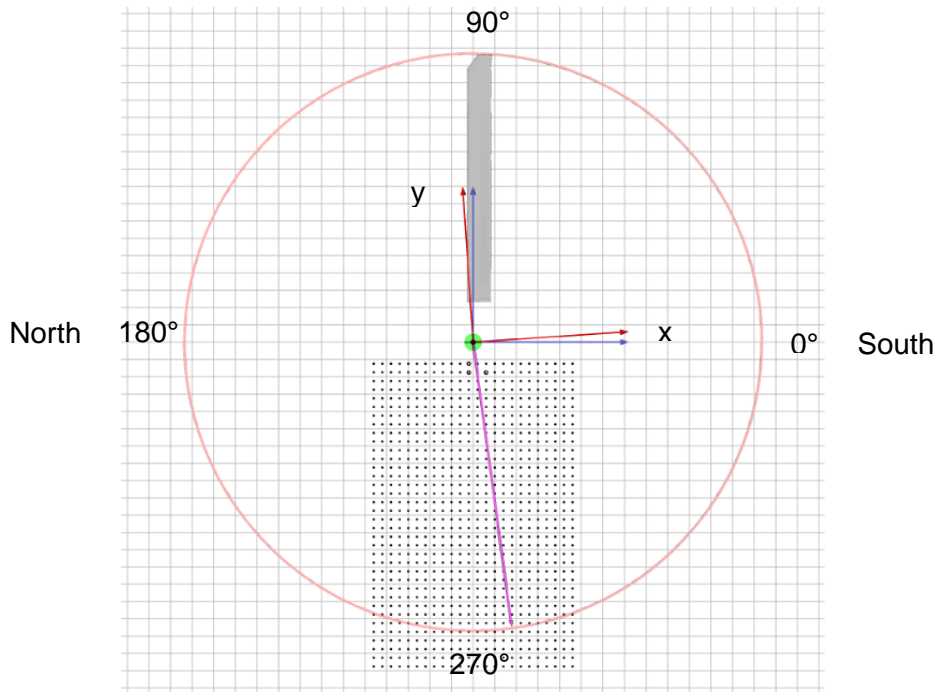


Figure 2. Tunnel coordinate axes showing one blade and target-board targets. The view is from above; z is out of the page; rotation is counter-clockwise. The red axes indicate the misalignment of the encoder.

3. Test article

3.1 Rotor blades and test stand

The test article was a four-bladed rotor that was supported by the Army Rotor Test Stand (ARTS⁷) on a mast that placed the rotor plane 40 feet above the floor of the test section (Fig. 3). The diameter of the rotor was 11.08 feet, and the rotor blades were the HVAB blade set. These blades use a Government RC-series of airfoils and had a linear twist distribution of -14° . The blades were of constant chord (5.45 in) and un-swept except for the outboard 5% where the leading edge was swept back 30° and the chord at the tip was 3.27 inches (Fig. 4). The rotor blades were fully articulated with the flap and lead-lag hinge co-located 3.5 inches from the rotor shaft. The elastic axis was at the quarter chord. The blades were coated with high-emissivity black polyurethane paint to accommodate IR thermography. The rotor was driven by two 200 HP electric motors. Rotor RPM was derived from the output of a 1024-per-rev optical encoder at the base of the test stand. Details about the drive system and instrumentation in the ARTS may be found in Ref. 2.

The HVAB blade set consisted of six blades: one blade that was instrumented with 187 unsteady pressure transducers (SN004); a second blade with 51 unsteady pressure transducers

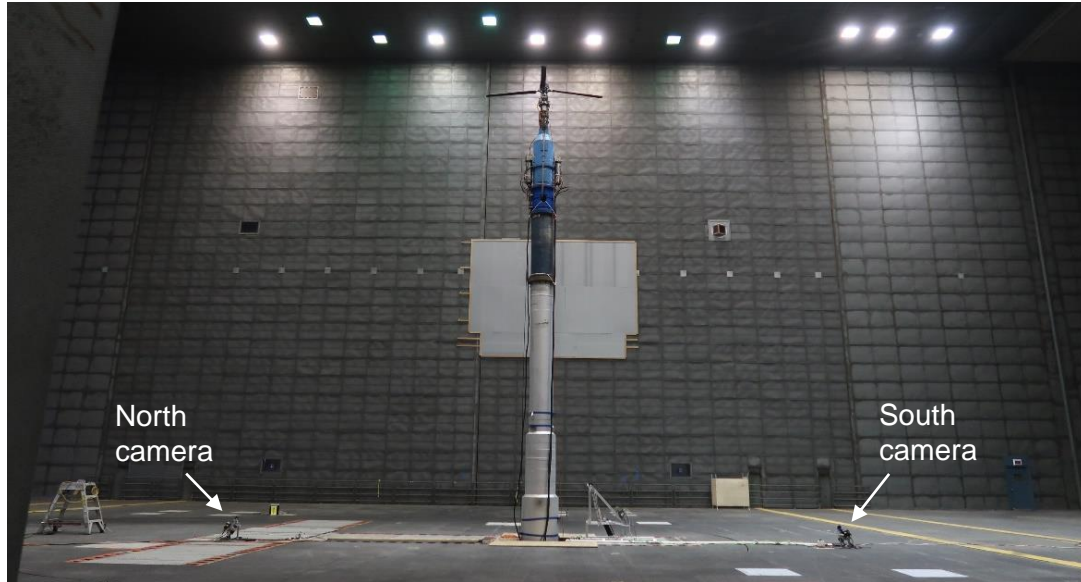


Figure 3. Placement of photogrammetry cameras.

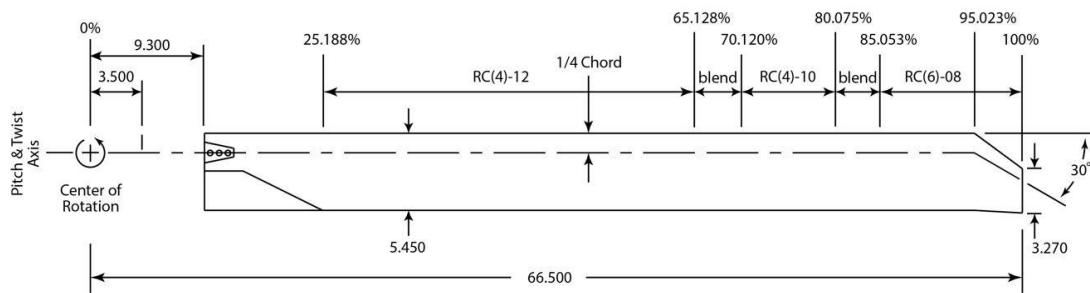


Figure 4. Rotor blade planview.

(SN006); three “standard” blades with no instrumentation except strain gauges near the root ($r/R = 0.253$) (SN001, SN002, SN003); and one blade with four sets of strain gauges along the span of the blade ($r/R = 0.253, 0.40, 0.60, 0.825$) (SN005). Dummy transducers and wiring were installed in the three standard blades at the same locations as real transducers in blade SN004 in order to best match the mass distribution and structural properties of SN004. All blade-displacement measurements were made when the rotor was composed of the three standard blades (SN001, SN002, SN003) and SN005. The order of blade passage was SN005, SN002, SN003, SN001. There were no deformation measurements of either of the pressure-instrumented blades. Details of the blades’ structural and geometric properties may be found in Ref. 1.

3.2 Targets

Eighty adhesive, retro-reflective targets punched from sheets of 3M 7610 material were applied to the lower surface of each blade. The targets were $\frac{1}{4}$ -inch in diameter and 0.005 inches thick; they were arranged in chord-wise rows of four at each of 20 radial stations (Fig. 5). By comparison, the UH60-A rotor had three targets per row at 16 radial stations, and the PSP rotor had only two targets per row at ten stations. We expected that the increased number of targets per row would reduce uncertainty in the elastic twist measurements.

The spatial coordinates of the targets were measured using a commercial photogrammetry system (V-STAR⁸). A dummy cuff supported each blade horizontally with its leading-edge

down to minimize bending due to gravity (Fig. 6). The angle at the blade root ($r/R = 0.14$) relative to the vertical direction was set to 8.2° , which corresponded to zero angle of attack (relative to vertical) at $r/R = 0.75$ and, by definition, zero collective pitch ($\Theta_0 = 0$). Six additional reference targets were applied to each blade at points near the root and tip where the “as-designed” coordinates in the blade coordinate system were known. The V-STARS measurements of all targets were translated to best match the as-designed coordinates of the



Figure 5. Targets on rotor blades.

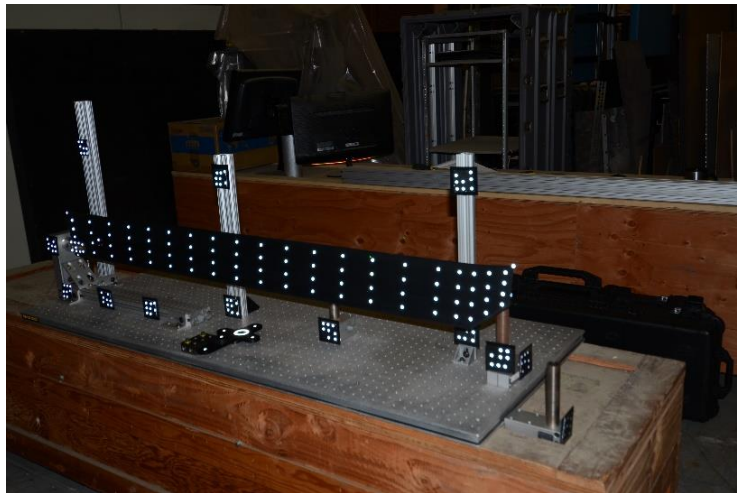


Figure 6. Setup for V-STARS measurements of unloaded blade.

reference targets. The blade coordinate system is shown in Fig. 7. The transformed V-STARS coordinates were the unloaded reference against which loaded measurements were compared. The targets were removed after the blade-deformation phase of the test was completed.

4. Photogrammetry system

4.1 Cameras and lamps

During testing the lower surface of each blade was imaged by two synchronized Dalsa 12M Falcon digital cameras (4096 x 3070 pixels, eight bits deep) as the blade passed through the 270 degree azimuth. The cameras were mounted on the floor of the test section equidistant (23 ft) north and south of the rotor mast and offset laterally (west) from the test section centerline by

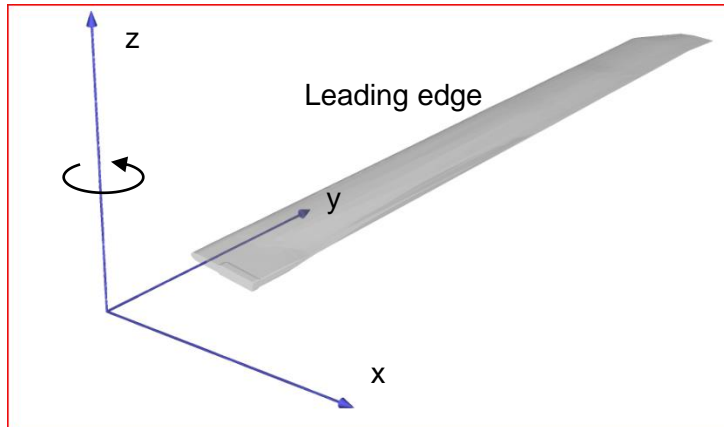


Figure 7. Blade coordinate system.



Figure 8. North camera and lamps mounted on the floor of the test section.

the rotor radius (Fig. 3). The angle between their optical axes was 60 degrees. Both cameras were fitted with an $f/2.8$ 180 mm focal length lenses which resulted in spatial resolution of the rotor of about 58 pixels per inch. The rotor was illuminated by six LED flash lamps, three co-located with each camera (Fig. 8). Four of the lamps were fitted with Fresnel lenses to concentrate the light at the measurement station.

The cameras and lamps were triggered by a once-per-rev signal that originated at the rotor shaft encoder. This signal was delayed by a Rotor Azimuth Synchronization Program (RASP)⁹ unit to place one of the four blades at the measurement station. The signal from the RASP was input to a digital pulse generator which allowed separate control of the widths of the pulses presented to the cameras and lamps. These pulse widths set the integration time of the cameras (50 μsec) and flash duration of the lamps (7 μsec), respectively. Each camera transmitted its images to a digital video recorder (DVR) across fiber-optic cables. The DVRs were controlled by a PC running IO Industries CoreView software. At each test point, images were acquired for 128 consecutive revolutions (“instances”) as other data were also being acquired.

4.2 Camera calibration

Camera calibration involves finding the coefficients of a transformation that maps points in 3D object-space to the 2D image plane of the camera. The cameras were calibrated using the collinearity equations, which assume a pinhole projection. Each point in 3D object space (x, y, z) is projected along a straight line through a pinhole lens and onto to the 2D image plane (X, Y) of the camera¹⁰:

$$\begin{aligned} X &= X_p - c_x \left[\frac{m_{11}(x - x_c) + m_{12}(y - y_c) + m_{13}(z - z_c)}{m_{31}(x - x_c) + m_{32}(y - y_c) + m_{33}(z - z_c)} \right] \\ Y &= Y_p - c_y \left[\frac{m_{21}(x - x_c) + m_{22}(y - y_c) + m_{23}(z - z_c)}{m_{31}(x - x_c) + m_{32}(y - y_c) + m_{33}(z - z_c)} \right] \end{aligned} \quad (1)$$

where (X_p, Y_p) is the principal point (where the optical axis passes through the image); (c_x, c_y) are horizontal and vertical image scale factors (proportional to focal length), respectively; (x_c, y_c, z_c) is the perspective center (camera position); and m_{ij} is a 3x3 rotation matrix whose elements are functions of the three camera point angles¹¹. (X, Y) are image-plane coordinates after correction for lens distortion. They are computed from measured coordinates (X_d, Y_d) by¹²:

$$\begin{aligned} X &= X_d - K_1(X - X_p)r^2 - K_2(X - X_p)r^4 \\ Y &= Y_d - K_1(Y - Y_p)r^2 - K_2(Y - Y_p)r^4 \end{aligned} \quad (2)$$

where $r^2 = (X - X_p)^2 + (Y - Y_p)^2$ and K_1 and K_2 are first- and second-order symmetrical lens distortion correction factors. Taken together, (X_p, Y_p) , (c_x, c_y) , and (K_1, K_2) are the internal orientation of the camera; and (x_c, y_c, z_c) and m_{ij} are the external orientation or pose. Each camera was calibrated in two steps: first the internal orientation was measured, followed by the external orientation.

4.2.1 Internal orientation

The internal orientation of each camera was computed independently by Zhang's method¹³. After each camera had been focused on a static rotor blade in the region of interest ($\psi = 270^\circ$), a sequence of images of a flat target board was acquired where in each image the board was at a different orientation relative to the camera (e.g., normal to the optical axis; yawed $\pm 45^\circ$; pitched $\pm 45^\circ$; rotated 90° ; etc.). The target board was four feet by six feet with a rectangular array of circular targets spaced at two-inch intervals in both directions. Because of the difficulty in supporting this board at many orientations in the region of interest (40 feet in the air), the image sequence was acquired after re-pointing the cameras horizontally and hand-holding the board on the floor at the camera-to-region-of-interest distance. The internal orientation was computed from the image-plane coordinates of targets in all of the images.

4.2.2 External orientation

After the internal orientation images had been acquired, the cameras were re-pointed at the region of interest, and the same flat target board was supported horizontally in the rotor plane by a special fixture attached to the test stand (Fig. 9). The position and orientation of the board established the coordinate system of the photogrammetry measurements and were set to be approximately the same as the true tunnel axes (Fig. 2). The board was levelled in the pitch and roll directions using a digital inclinometer. The in-plane rotation of the board (yaw) was set so that rows of targets were approximately aligned to the tunnel axis. Likewise, the height of the board was approximately in the rotor plane, and the lateral position was arbitrary. It was not essential for these coordinates to be precisely aligned to the true tunnel axes because the

photogrammetry measurements were always transformed to the blade coordinate system (Fig. 7) where blade deformation was measured. Once the target board was in position, a single image was acquired with each camera, and targets in the images were located. Then, using the

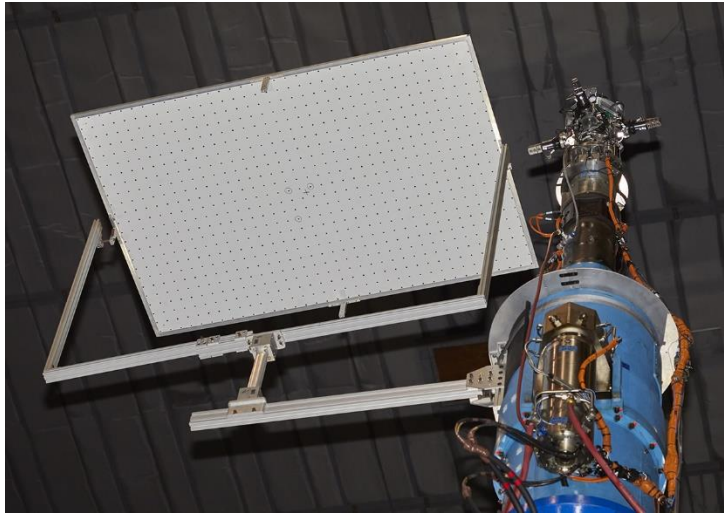


Figure 9. Target board mounted on the test stand for camera pose calibration.

known internal orientation of the camera and a guess of the pose, the known 3D position of each target (in target-board coordinates) was projected into the image of each camera (Eq. 1), and the projected pixel coordinates were compared to the actual coordinates measured in the images. The pose parameters were adjusted iteratively to minimize the root-mean-square re-projection errors of all targets. This was a nonlinear optimization problem that was solved using the Levenberg-Marquardt algorithm¹⁴.

5. Data Acquisition

5.1 NFAC Data Acquisition System

Most of the non-optical data, including balance (force and moment) data and pitch, flap, and lag measurements, were acquired by the NFAC Data Acquisition System (DAS). For this test, data were sampled at 256 samples per revolution ($\Delta\psi = 1.4^\circ$) averaged over 128 revolutions. Both DAS and photogrammetry measurements were triggered by a once-per-rev signal from a 1024 counts-per-rev optical encoder mounted to the rotor shaft. Data acquisition by the two systems overlapped but did not necessarily begin on the same revolution because acquisition by each system was independently initiated by separate operators upon hearing a “take data” command.

By design, the zero reference pulse from the optical encoder occurred when the first blade (SN005) was pointed nominally south (aligned with the tunnel axis). Because of an encoder misalignment, however, this pulse actually occurred 3.86° beyond this position. The effects of this misalignment are described in the next section.

Pitch, flap, and lag of each blade were measured independently. Pitch was measured by a Hall Effect sensor mounted to a bracket attached to the blade spindle. Flap and lag were measured by potentiometers mounted to the hinge block. The pitch and flap sensors were calibrated against digital inclinometers. The lag sensors were calibrated against reference marks machined at 5° intervals on the rotor hub.

5.2 Photogrammetry data acquisition

Blade deformation measurements were made during three “research” runs at tip Mach numbers of 0.60, 0.65, and 0.675, respectively. In each run, the collective pitch was stepped in 2° increments to angles between 4° and 14°. At each angle the RASP was set to trigger the cameras when one of the blades (beginning with SN002) passed through the measurement azimuth ($\psi = 270^\circ$). Then, on a “take data” command, separate operators initiated the recording of images and DAS data from 128 consecutive revolutions. After five such measurements of the current blade (with a 3-5 second delay between measurements), the RASP was advanced 90° and the process was repeated for the next blade. Once measurements of all four blades at the current pitch had been completed, the collective pitch was stepped to the next value, and the entire process was repeated until measurements at the last collective pitch had been acquired. Blade-displacement research runs typically lasted 1½–2 hours.

To minimize the effect of thermal drift on the balance data, each research run was preceded by a “pre-heat” run that lasted until the balance data had stabilized (30–45 minutes). This significantly increased the time that the adhesive retro-reflective targets were exposed to shear stresses due to skin friction and centrifugal force, which were greatest at the blade tips. As a consequence, research runs usually began with several targets missing near the blade tips.

It was known that the rotor shaft encoder was misaligned with respect to true tunnel axes by 3.86° in the counter-clockwise direction (looking down, Fig. 2). Intending to correct for this offset so the cameras would be triggered at $\psi = 270^\circ$, we mistakenly set the RASP to trigger at $\psi = 270^\circ + 3.86^\circ = 273.86^\circ$ whereas we should have set it to $\psi = 270^\circ - 3.86^\circ = 266.14^\circ$. As a consequence, the cameras were actually triggered at $\psi = 273.86^\circ + 3.86^\circ = 277.72^\circ$ in true tunnel coordinates. At this azimuth the blades were slightly closer to the south camera than to the north camera. This difference increased the brightness of targets in images from the south camera and reduced their brightness in images from the north. The targets in the images from the north camera were already somewhat dimmer because, at positive collective pitch, the illumination of the lower surfaces by the flash lamps was more oblique and retro-reflection from the targets was less efficient. Otherwise the error in setting azimuth was of no consequence, because the rotor was in hover.

6. Photogrammetry data reduction

Photogrammetry data reduction is the process by which blade deformation measurements are extracted from the images of both cameras. For this test, this was accomplished using software developed in house and consisted of the following steps:

1. Locate all targets in the images from both cameras.
2. Compute the 3D space coordinates of all targets at each instance.
3. Compute the six-degree-of-freedom rigid-body transformation between loaded and unloaded conditions.
4. Apply the rigid-body transformation to the 3D coordinates of all targets, bringing them into blade reference coordinates.
5. Compute bending and elastic twist from loaded and unloaded 3D coordinates in blade reference coordinates.
6. Compute average and standard deviation of 128 instances at each test point.

6.1 Locate targets

Target finding was a semi-automatic, two-step process. The first step was to define the approximate positions of all targets, either manually by point and click with the computer mouse, or automatically using target locations from a previous test point. The second step was to refine the approximate positions using an automatic target finder that searched within a rectangular window centered on the approximate location of each target. The target finder was a “blob

detector” that established a closed perimeter around contiguous pixels that were brighter than a user-input threshold (for bright targets on a dark background). If the length of the perimeter lay between user-input limits, the target was accepted, and its position was computed as the centroid of pixels within the perimeter. A third step—manually correcting incorrectly located targets—was also often necessary. Once the targets were located in the first image of a 128-image sequence, target finding in the following images was fully automatic.

6.2 Compute 3D coordinates

The space coordinates (x, y, z) of each target were computed at each instance from the pixel coordinates (X, Y) of the target in the images of both cameras (A and B) and the internal and external camera calibration coefficients¹²:

$$\begin{bmatrix} a_1^A & a_2^A & a_3^A \\ a_4^A & a_5^A & a_6^A \\ a_1^B & a_2^B & a_3^B \\ a_4^B & a_5^B & a_6^B \end{bmatrix} \times \begin{bmatrix} x \\ y \\ z \end{bmatrix} = \begin{bmatrix} a_1^A x_c^A + a_2^A y_c^A + a_3^A z_c^A \\ a_4^A x_c^A + a_5^A y_c^A + a_6^A z_c^A \\ a_1^B x_c^B + a_2^B y_c^B + a_3^B z_c^B \\ a_4^B x_c^B + a_5^B y_c^B + a_6^B z_c^B \end{bmatrix} \quad (3)$$

where

$$\begin{aligned} a_1 &= (X - X_p)m_{31} + c_x m_{11} \\ a_2 &= (X - X_p)m_{32} + c_x m_{12} \\ a_3 &= (X - X_p)m_{33} + c_x m_{13} \\ a_4 &= (Y - Y_p)m_{31} + c_y m_{21} \\ a_5 &= (Y - Y_p)m_{32} + c_y m_{22} \\ a_6 &= (Y - Y_p)m_{33} + c_y m_{23} \end{aligned}$$

The image-plane coordinates (X, Y) were corrected for first- and second-order symmetrical lens distortion (Eq. 2). Equation 3 is an over-determined set of linear equations that was solved in a least-squares sense for (x, y, z). The computed space coordinates of all targets were in the coordinate system established by the target board for the external calibration. The least-squares solution includes an error which is one measure of the uncertainty. Another measure is the re-projection error which can be computed for each camera by substituting the least-squares solution for (x, y, z) of a target into Eq. 3 and comparing the resulting computed pixel coordinates to the observed coordinates of the target in each image. In the present test the RMS of re-projection errors computed for all targets was typically 1–1.5 pixels.

6.3 Compute rigid-body transformation

The rigid-body transformation between the loaded and unloaded conditions was computed at each instance by comparing the spatial coordinates of a set of rigid-body targets at both conditions and finding the rigid-body displacements and rotations that gave the best match. This is a nonlinear least-squares problem that was solved using the Levenberg-Marquardt algorithm. The unloaded spatial coordinates of the targets were those measured by V-STARS and were in the blade coordinate system (Fig. 7). Knowing the position of the hinge ($r = 3.5$ in), the angle of the rotor shaft (0°), and the azimuth of the measurement station (nominally $\psi = 270^\circ$), the rigid-body rotations from tunnel (pose target board) to blade coordinates were resolved into pitch (Θ), flap (β), and lag (ζ) angles, applied in that order.

Defining rigid-body targets on a flexible rotor blade is problematic. Our baseline was to assume that the most inboard three rows of targets ($r/R \leq 0.25$) were rigidly connected. Then, to assess the sensitivity of the solutions to this assumption, the calculations were repeated using four ($r/R \leq 0.30$) and five ($r/R \leq 0.35$) rows as rigid.

6.4 Transform targets to blade coordinates and compute bending and elastic twist

Once the rigid-body transformation was computed, it was applied to all targets, taking them from the target-board to the blade coordinate system. After this transformation, differences between the loaded and unloaded spatial coordinates of all targets were assumed to be due to bending and elastic twist. Bending was displacement in the out-of-plane (z) direction in blade coordinates and at each radial station was interpolated to the elastic axis (quarter chord). The elastic twist at each radial station (computed from the four targets at each station) was rotation about the radial axis. Finally, the average and standard deviation of 128 instantaneous measurements were computed to represent a single data point.

6.5 Details on elastic twist and “real-world” issues

Elastic twist at each radial station was computed from the loaded and unloaded space coordinates of the four targets at that station. This was accomplished by finding the rigid-body transformation that, when applied to the unloaded target coordinates, gave the best fit to the loaded target coordinates. Rotation about the y axis (blade coordinates) was interpreted as the elastic twist at that station.

An alternate method for computing elastic twist was to compute the out-of-plane displacements (Δz) of all four targets at each span station (y) and find the slope of the linear best fit of Δz versus x. By this method, elastic twist = $-\tan^{-1}(\Delta z/\Delta x)$. Differences in twist computed by both methods were very small.

Well in advance of the test, we demonstrated that we could measure elastic twist to within 0.1° on a static object at the full scale of the test. For convenience, the two cameras with lamps and the test object were positioned in a horizontal plane (on the floor of a large room) at the same relative positions that they would have in a vertical plane when installed in the test section (46 ft between the cameras; 40 ft from the camera baseline to the test object). The first test object was a small target board mounted to a micrometer-driven rotary stage. Later, measurements were made of one of the PSP rotor blades where a torque was applied about the elastic axis. The resulting elastic twist was independently measured by photogrammetry and by digital micrometers that measured displacements at the leading and trailing edges of the blade. This setup was also used to (1) confirm that integration times (flash-lamp pulse widths) as short as $10 \mu\text{s}$ (needed to freeze the motion of the blade) resulted in images of the retro-reflective targets that were sufficiently bright; and (2) explore the benefits of adding targets at each radial station.

Several “real-world” issues complicated the acquisition and analysis of the photogrammetry measurements. The most serious was loss of targets. In the two rows nearest the tip ($r/R \geq 0.95$), several targets on each blade often became detached under shear stress and centrifugal loading; and in the most inboard row ($r/R = 0.15$), the brightness of two targets on each blade was often diminished due to grease contamination from the blade-cuff junction. Although lost targets were replaced before each run, they were often lost again during the long pre-heat runs that preceded each research run. A stronger adhesive might have solved this problem but was not used because the solvent necessary to remove the targets afterward would likely have damaged the underlying black paint, which needed to be preserved for thermography. At rows where targets were missing, whether by detachment or contamination, the elastic twist computed from the remaining targets in that row (which sometimes was only two closely spaced targets) was often unreliable. Therefore, elastic twist measurements at these stations have been omitted from the final database.

Another issue was that the interval between once-per-rev pulses from the encoder alternated between 1023 and 1024 counts. Since the photogrammetry cameras were triggered by the encoder, the true azimuths of the blades in odd- and even-numbered images differed by $1/1024 \times 360^\circ = 0.35^\circ$. Ideally in hover, blade displacement is independent of azimuth, so this

difference would be of no consequence; however, it introduced “jitter” of the blade in the stream of even and odd images.

7. Test results

Our goal was to compile a database of blade deformation measurements that can be used by analysts to validate their codes. For an idealized rotor in hover, blade deformations should be independent of time and azimuth, and the deformation of all blades should be identical. Therefore, a database describing the deformation of an idealized rotor in hover need only tabulate bending and elastic twist of a single blade at each combination of RPM and collective pitch. In addition, rigid-body rotations of all blades should be the same and can be described by pitch, flap, and lag angles.

Because an idealized rotor does not exist in practice, we measured each blade separately over many revolutions and averaged the average deformation of all four blades. This procedure mitigated blade-to-blade differences as well as point-to-point differences due to unsteady recirculation.

We begin by showing data for a single blade at a typical, single test condition. We then show repeated measurements of each blade at the same test condition and compare the averages of each. Finally, we average the average measurements of all four blades and show the effects of changes in collective pitch and rotor RPM.

7.1 A single test point

Figure 10 shows a typical image from each camera at 1250 RPM and $\Theta_0 = 12^\circ$. The targets appeared bright against a nearly black background and showed minimal chord-wise elongation due to rotation. The baseline rigid-body targets are indicated by the yellow ellipses. Missing targets—one each in the two rows closest to the tip that became detached, and two at the most inboard row that were contaminated by grease—are indicated by red ellipses. In Fig. 11, an image of blade SN002 from the south camera is overlaid by a color map that shows average bending data for a single test point (average of 128 consecutive revolutions). Figure 12 shows bending versus r/R along each of the four chord-wise columns of targets. At all span stations bending displacements are smallest near the leading edge and increase with increasing

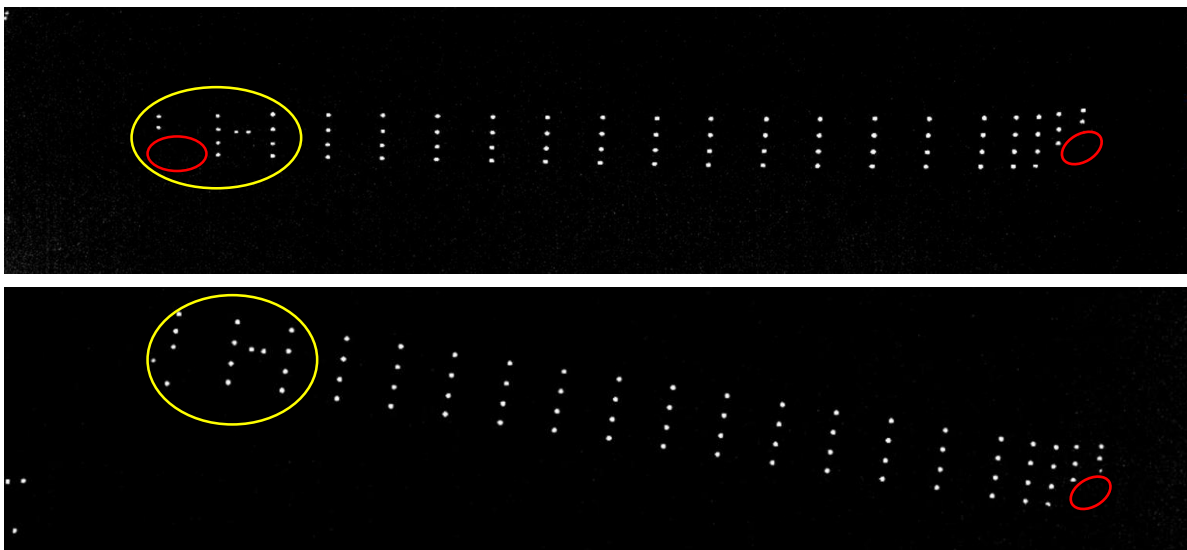


Figure 10. Typical images (cropped) of blade SN002 from North (top) and South (bottom) cameras showing baseline rigid-body targets (yellow) and missing targets (red) (root to the left, tip to the right). South image has been rotated to facilitate comparison to North image).

distance from the leading edge—consistent with nose-down elastic twist. The RMS re-projection error of all targets in all images from both cameras was about 1.2 pixels. This was typical for all measurements.

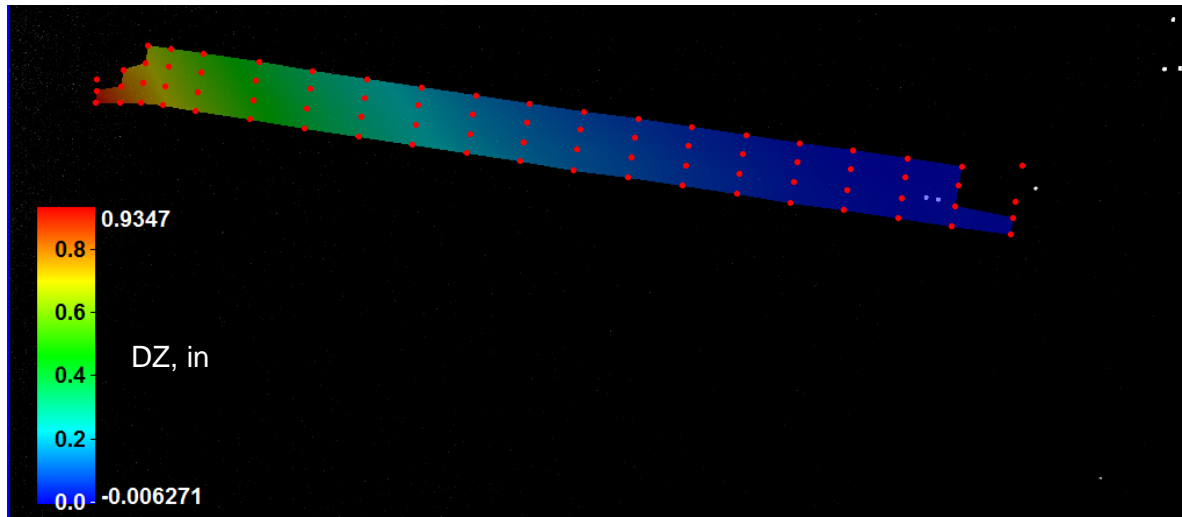


Figure 11. Image from South camera with overlay of targets and out-of-plane bending data (1250 RPM, $\theta_0 = 12^\circ$, SN002). Note data drop-outs due to missing targets near the tip (left).

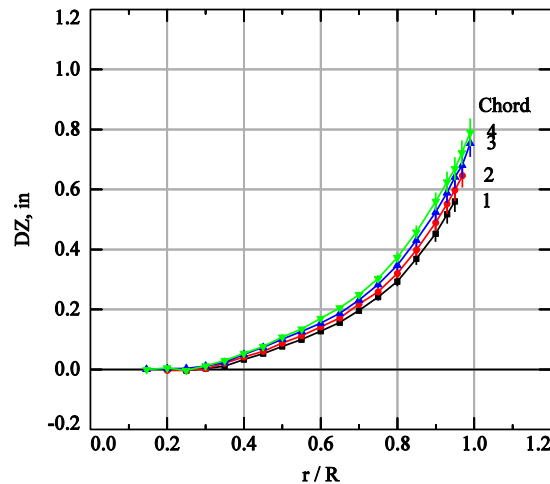


Figure 12. Bending versus r/R at four chord-wise positions (1250 RPM, $\theta_0 = 12^\circ$, SN002)

7.2 Repeated test points

Figure 13 shows five repeated measurements of DZ versus chord-wise position (x) for blade SN002 at the same test conditions (1250 RPM, $\theta_0 = 12^\circ$). The targets are located at span station 18 ($r/R = 0.95$, just inboard of the swept tip). The displacements increase linearly from the leading to the trailing edge, and the positive slopes of the lines can be interpreted as negative (nose down) elastic twist. Variations in bending among the measurement points are indicated by the different DZ offsets. The slopes of DZ versus x are nearly the same for all five repeat points.

Five repeated measurements of bending and elastic twist of blade SN002 at the same test condition are shown in Fig. 14. Bending measurements at each span station were interpolated to the quarter chord. Error bars at each point indicate \pm one standard deviation of the 128 instantaneous measurements. Each test point shows a smooth progression of both bending and elastic twist as functions of radius (r/R). There are, however, significant differences among the

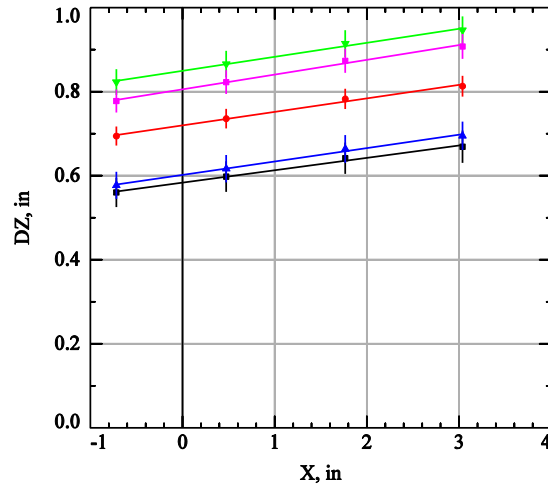


Figure 13. Variation of five repeated measurements of bending versus chord-wise position (x) at $r/R = 0.95$ (1250 RPM, $\theta_0 = 12^\circ$, SN002). Positive slope indicates nose-down elastic twist.

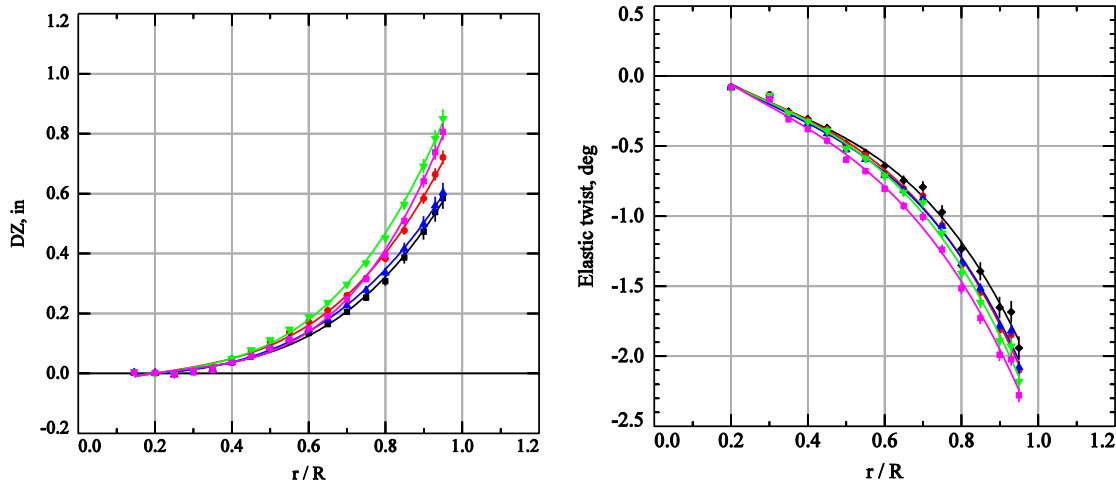


Figure 14. Variation of five repeated measurements of bending (left) and elastic twist (right) (1250 RPM, $\theta_0 = 12^\circ$, SN002).

repeated measurements. Differences in bending at the tip were as large as 0.3 inches, and differences in elastic twist were as large as 0.5° .

Repeated measurements of the other three blades showed similar differences as blade SN002.

7.3 Blade-to-blade comparisons

Blade-to-blade comparisons of bending and elastic twist at the same test condition (1250 RPM and $\theta_0 = 12^\circ$) are shown in Fig. 15. Data for each blade have been averaged over five repeated test points. Error bars indicate \pm one standard deviation of the five average measurements. The average bending of each blade varied smoothly with radius, and

differences in bending among the blades at each radius were less than 0.1 in. Blade-to-blade differences in average elastic twist measurements were less than 0.5°.

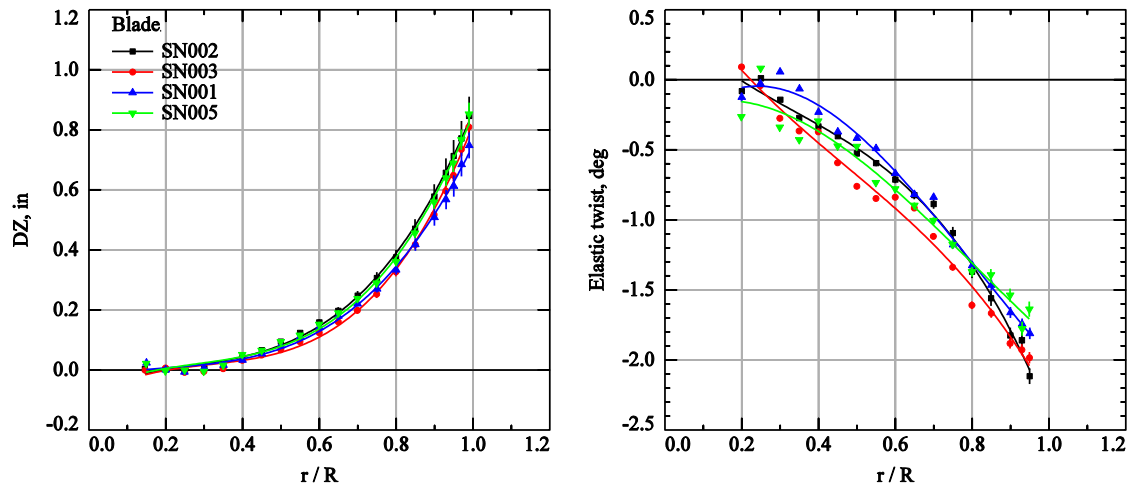


Figure 15. Blade-to-blade comparison of measurements of bending (left) and elastic twist (right) (1250 RPM, $\theta_0 = 12^\circ$, SN002).

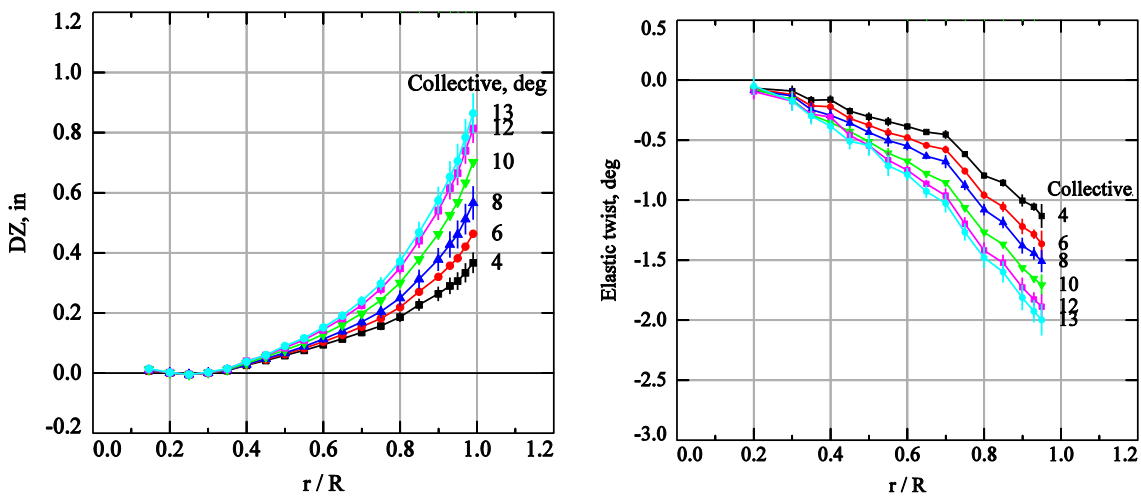


Figure 16. Effect of collective pitch set point on bending (left) and elastic twist (right) versus r/R . Measurements were averaged over four blades (1250 RPM).

7.4 Effects of collective pitch and RPM

In Fig. 16 the average bending and elastic twist of all four blades are plotted versus radius for collective pitches between 4° and 13° at 1250 RPM. Error bars show \pm one standard deviation of the 20 test points (5 repeats per blade x 4 blades) that were averaged. As expected, upward bending increased monotonically with increasing collective pitch whereas elastic twist became more negative.

Figure 17 shows the effect of increasing RPM on bending and elastic twist at $\theta_0 = 12^\circ$. Data at each RPM are the average 20 test points (average of four blades each repeated five times). RPM had a greater effect on elastic twist than on bending: elastic twist became increasingly nose down (negative) as RPM increased with a maximum difference at the tip of about -0.5°;

bending changes were small (about 0.1 inches near the tip) and were not monotonic. The same trends were evident at lower collective pitches.

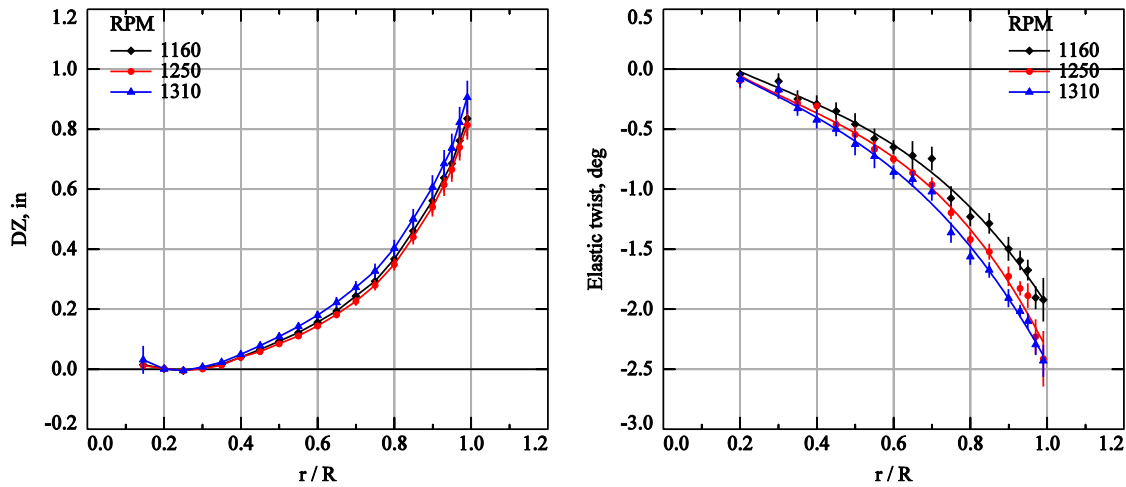


Figure 17. Effect of RPM on bending (left) and elastic twist (right) versus r/R . Measurements are averaged over four blades ($\theta_0 = 12^\circ$).

7.5 Pitch, flap, and lag

Root pitch, flap, and lag angles were by-products of blade deformation measurements. They were the three rotations required to transform the rigid-body targets 3D locations from target-board (Fig. 2) to blade coordinates (derived from V-STARS measurements). Pitch, flap, and lag angles were also independently measured by the DAS. In Fig. 18, the blade-displacement measurements (photogrammetry) are plotted versus the DAS measurements for all four blades at all test points at 1250 RPM. Slopes and offsets of the linear fits of the data are tabulated in Table 1 (Appendix).

Except for small offsets, the blade-displacement measurements of pitch were in good agreement with the DAS measurements for all four blades at all test points. This adds credibility to measurements of elastic twist, which is rotation about the same axis. Flap measurements showed considerably more point-to-point and blade-to-blade scatter, although the slopes were close to one (Table 1). Finally, there was poor agreement between photogrammetry and DAS measurements of lag: there were large offsets in the photogrammetry measurements relative to DAS that were likely due to misalignment of the target board with respect to the tunnel axes. The slopes of photogrammetry vs. DAS measurements for blades SN002, SN003, and SN005 were nearly the same as each other but significantly larger than 1. The slope for blade SN001 was even larger, indicating a significant scaling discrepancy. This discrepancy has not been explained.

8. Discussion

The following section provides a discussion of the photogrammetry data repeatability and uncertainty for individual measurements as well as some lessons learned. In spite of the rather large variations of individual measurements noted below, the averaging process used for the final data provides reasonably accurate results for validation.

8.1 Repeatability

Each photogrammetry measurement was the average of 128 consecutive once-per-rev measurements, and each measurement was repeated five times. There were significant

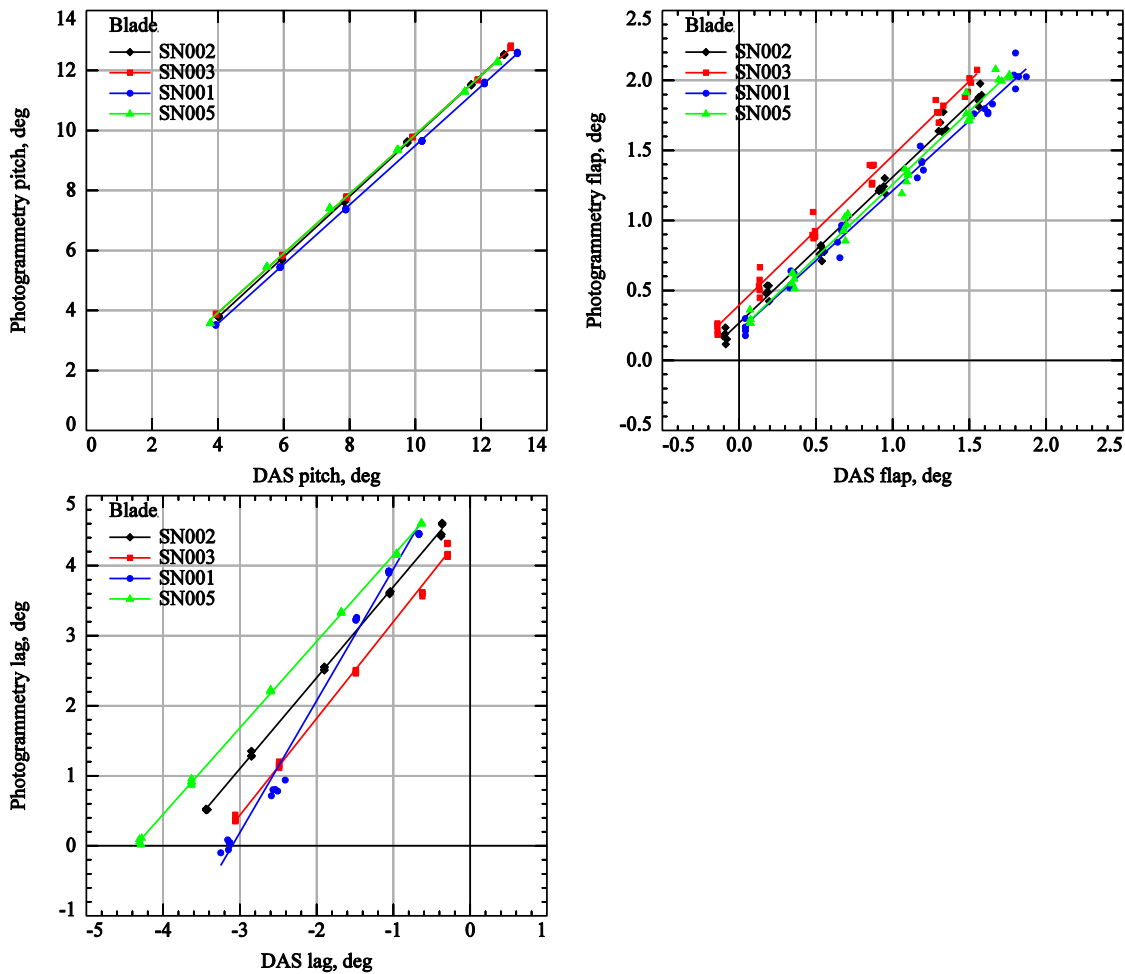


Figure 18. Pitch (top-left), flap (top-right) and lag (bottom) measurements of four blades: photogrammetry versus DAS (1250 RPM).

differences between average values among repeated measurements of bending and elastic twist acquired at ostensibly the same test conditions. Likewise, differences in average bending and elastic twist among the four blades were larger than expected. However, metrics used to assess the uncertainty of individual photogrammetry measurements (e.g., re-projection errors and residuals of Eq. 3) indicated that the uncertainties were small. To better understand why these differences occurred, we examine typical time histories of the repeated measurement points.

8.1.1 Cycle-to-cycle “jitter”

As we have noted, the 1024 counts-per-rev encoder that triggered the photogrammetry cameras appeared to drop one count every other revolution. This caused the azimuth of each blade to differ at even and odd cycles by $360 / 1024 = 0.35^\circ$. As a result the blades appeared to jitter back and forth in the image sequence. This is shown in Fig. 19 (top-left) where the Y pixel coordinate of a target near the tip ($r/R = 0.97$) is plotted versus time for a single test point (128 consecutive revolutions, 1250 RPM, $\Theta_0 = 12^\circ$, blade SN002). Note that the periodic target position is modulated. The reason for this modulation is not understood. Figure 19 (top-right) shows, for the same test point, the in-plane, chord-wise spatial coordinate (x) of the same target. The same jitter and modulation are evident. It makes sense that the x coordinate would show this periodicity because at azimuth near 270° , variations in azimuth are in the longitudinal

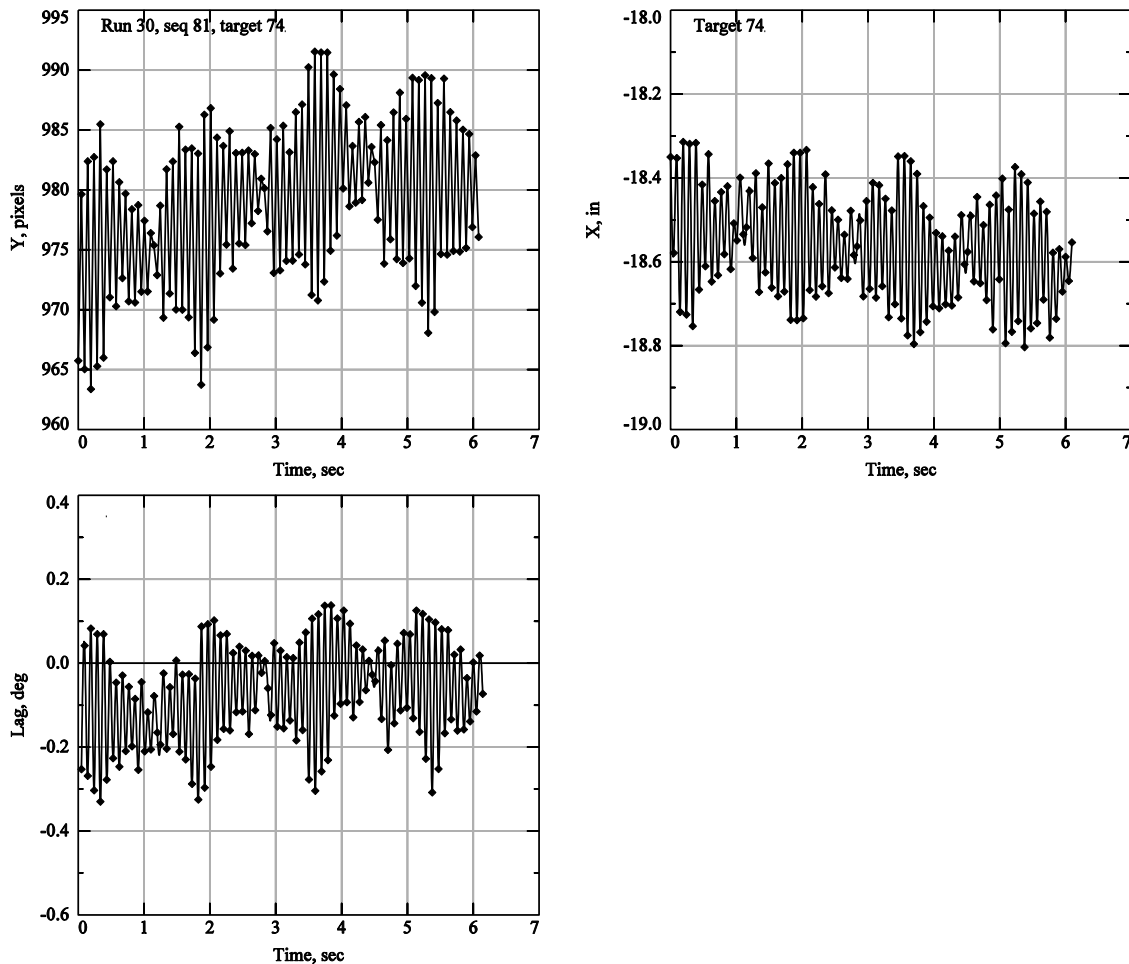


Figure 19. “Jitter” in time histories during a single test point of image Y (top-left), space x (top-right) of a target near the tip ($r/R = 0.97$). Time history of lag is shown at bottom-left (1250 RPM, $\Theta_0 = 12^\circ$, blade SN002).

(x) direction. Likewise, rigid-body lag for the same test point (Fig. 19, bottom-left) is in the longitudinal direction and shows the same behavior. The amplitude of the lag jitter is about 0.35° , the angular equivalent of one encoder count.

In spite of all the trouble that it caused, jitter had no effect on the bending and elastic twist measurements. This was confirmed for a typical case by comparing solutions computed from only even and only odd images.

It should be noted that the infrared cameras used for thermography were also triggered by the same encoder signal but did not exhibit the jitter evident in the photogrammetry images. Those cameras made use of both A and B outputs of the encoder thereby quadrupling the resolution and lessening the effect of dropped counts.

8.1.2 Bending measurement repeatability

Figure 20 (left) shows bending displacement (DZ) versus time of four targets at different radial stations during a single test point (1250 RPM and $\Theta_0 = 12^\circ$, blade SN002). The time histories are not random and appear to meander in small steps along deterministic paths. At $r/R = 0.97$, the range of bending is between 0.5 and 0.8 inches. Photogrammetry appears to have resolved out-of-plane displacements smaller than 0.05 inches. Figure 20 (right) shows the time history of bending at the most outboard target ($r/R = 0.97$) over five repeated test points.

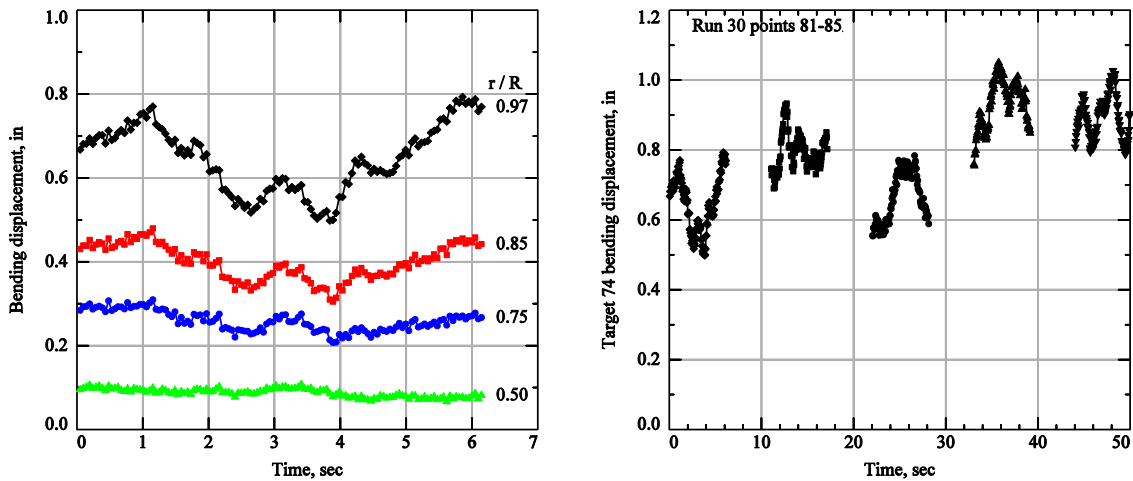


Figure 20. Time histories of bending at four radial stations during a single test point (left); and, for $r/R = 0.97$, at five repeated test points (1250 RPM, $\theta_0 = 12^\circ$, blade SN002).

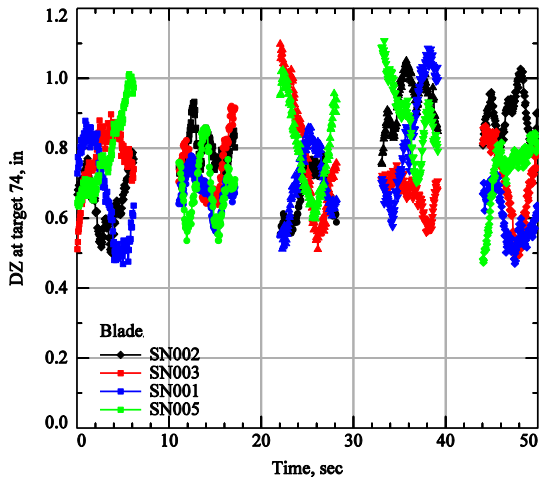


Figure 21. Blade-to-blade comparisons of time histories of bending at $r/R = 0.97$ over five repeated test points (1250 RPM, $\theta_0 = 12^\circ$).

The test points are separated by five-second gaps, which was the approximate time between test points. The data for the first test point ($0 < t < 6$ sec) are the same as shown in Fig. 20 (left) for $r/R = 0.97$. At each test point the data follow a winding, non-random path, and each path has a range of about 0.25–0.3 inches. Each path is different, and there are significant differences among their average values.

Figure 21 shows bending versus time at $r/R = 0.97$ of each of the four blades during the first data point of each (1250 RPM, $\theta_0 = 12^\circ$). Data for blade SN002 are the same as shown for $r/R = 0.97$ in Fig. 20. Although the data from each test point are overlaid in the same time intervals, the measurements of all blades were not made at the same times. Rather, measurements of blade SN003 were made after the fifth repeat point of blade SN002, and so forth for blades SN001 and SN005. For all blades, the target displacements are not random and lie between $DZ = 0.5$ and 1.0 inches. Data evaluations during testing, including the use of large tufts near the tunnel walls, suggest that these low-frequency variations are due to unsteady flow recirculation in the test section.

8.1.3 Elastic twist measurement repeatability

Figure 22 (left) shows time histories of elastic twist at four radial stations of blade SN002 during a single test point; and, for $r/R = 0.93$, at five repeated test points (Fig. 22 right) (1250 RPM, $\theta_0 = 12^\circ$). The instantaneous measurements appear to resolve differences in elastic twist as small as 0.1–0.2 degrees, and all of the measurements lie in the range -1.3 to -2.4°. Blade-to-blade comparisons of elastic twist at $r/R = 0.93$ over five test points are shown in Fig. 23.

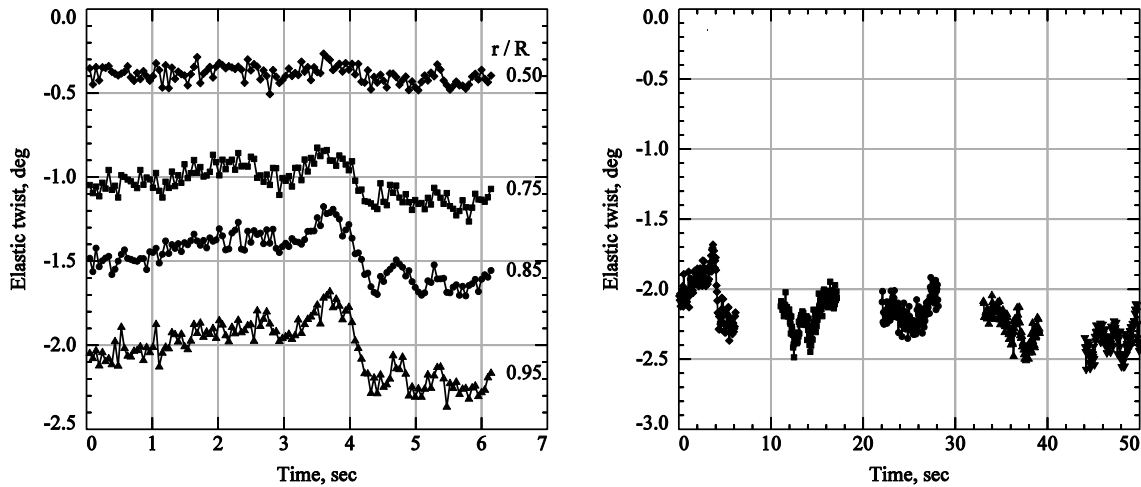


Figure 22. Time histories of elastic twist at four radial stations during a single test point (left); and, for $r/R = 0.95$, at five repeated test points (1250 RPM, $\theta_0 = 12^\circ$, blade SN002).

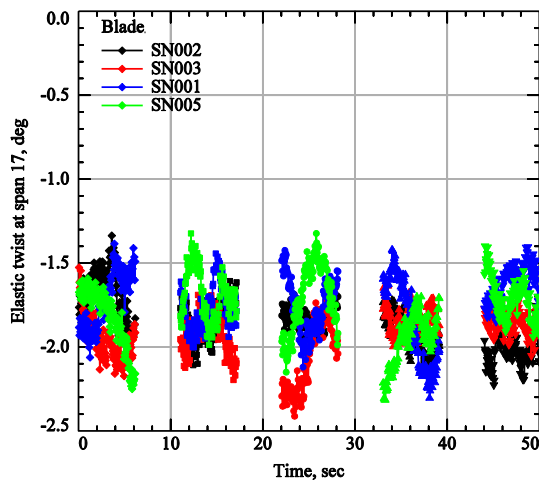


Figure 23. Blade-to-blade comparisons of time histories of elastic twist at $r/R = 0.93$ over five repeated test points (1250 RPM, $\theta_0 = 12^\circ$).

8.2 Uncertainty

Each measurement was the least-squares solution to a set of four equations and three unknowns (x , y , and z) and thus was not exact. The magnitude of the residual error can be interpreted as standard deviations of the measurement in the x , y , and z directions^{10, 12}. For a typical case, the standard deviation in the z direction was between 0.03 and 0.06 inches. The uncertainty of each measurement was also estimated by placing in the region of interest an object with two targets separated by a known distance. The separation of the targets in the z direction measured by photogrammetry agreed with the known separation to within 0.058 inches.

8.2.1 Random errors

The most likely source of random errors in bending and elastic twist measurements was random deviations in finding targets in the images. If we assume that that targets were located with an uncertainty of one pixel (a very conservative assumption—the uncertainty was more likely 0.1 pixels) and that these deviations at all targets were independent of each other, then the propagated uncertainty in bending and elastic twist from an instantaneous measurement near the tip was about 0.15 inches and 0.65°, respectively. This estimate is based on a quadrature error analysis: the image-plane position of each target that entered into the calculation of bending (or twist) was perturbed, one at a time; the resulting perturbation in bending (or twist) was computed and squared; and the square root was taken of the sum of the squares. For small errors, the propagated error scales linearly with the target-finding error, so for a more realistic target-finding error of 0.1 pixels, the random bending and elastic twist errors from a single measurement near the tip were about 0.015 inches and 0.065°, respectively.

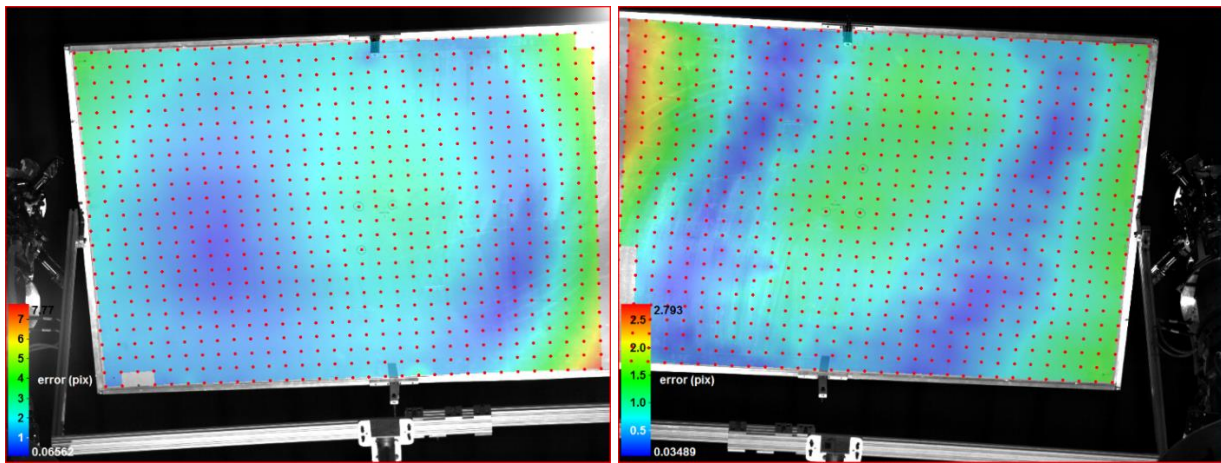


Figure 24. Pose calibration images from the North (left) and South (right) cameras with re-projection errors overlaid.

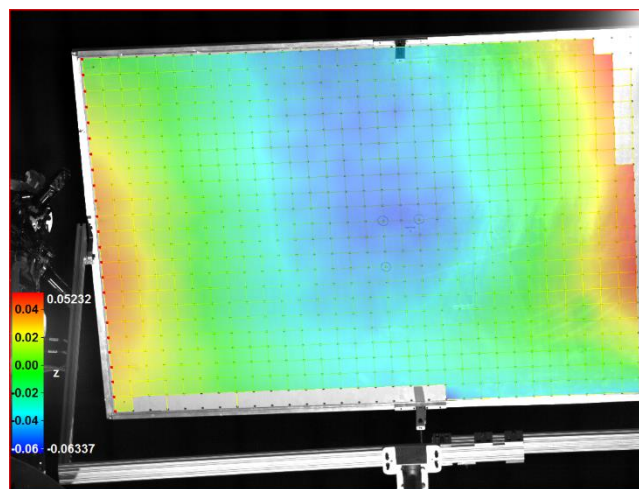


Figure 25. Pose calibration image from the North camera with z solution overlaid.

For a stochastic process, averaging the results of N repeated measurements reduces the random error by $1 / \sqrt{N}$. This was the rationale for repeating measurements 128 times at each

data point. As we have seen, however, the repeated measurements were deterministic, not stochastic, so averaging measurements did not reduce the random error—it averaged the effects of unsteadiness.

8.2.2 Bias errors

Bias errors in bending and twist will occur if there are bias errors in locating targets in the images. Some targets near the blade root were contaminated by grease and thus did not appear uniformly bright in the images. In some instances, one or more targets near the tip peeled up slightly at their leading edges resulting in images that were not ellipses.

Another important source of bias errors was imperfect camera calibration, i.e., the mapping from 3D object space to the 2D image plane of each camera (i.e., the camera calibrations, Eq. 1) did not perfectly represent the performance of the cameras. Figure 24 shows images of the pose calibration board from both cameras. Each image has been overlaid by a color map that shows the distribution of re-projection errors when the known space coordinates of targets on the plate (x and y at two-inch intervals, z uniformly zero) were projected into each image using Eq. 1 and the internal and external calibrations. The re-projection errors in each camera are small but not uniform. Figure 25 shows the z coordinates of all targets computed from the measured image coordinates and the camera calibrations (Eq. 2). The RMS error over all targets (i.e., deviations from $z = 0$) was 0.03 inches, and the maximum error was 0.065 inches. In-plane errors (x and y) were about half as large as these. Of course, the error in z assumes a perfectly flat plate (z uniformly 0), something that was not independently verified.

For blade deformation measurements, bias errors due to imperfect camera calibration would have subtracted out if the measurements at loaded and unloaded conditions had been made with the same cameras with the same bias errors. This was not the case, however, in the present test where target coordinates of the unloaded blades were measured by V-STARS (with negligible bias errors) and the targets of the loaded blades were measured by the two photogrammetry cameras (with bias errors as shown in Fig. 25).

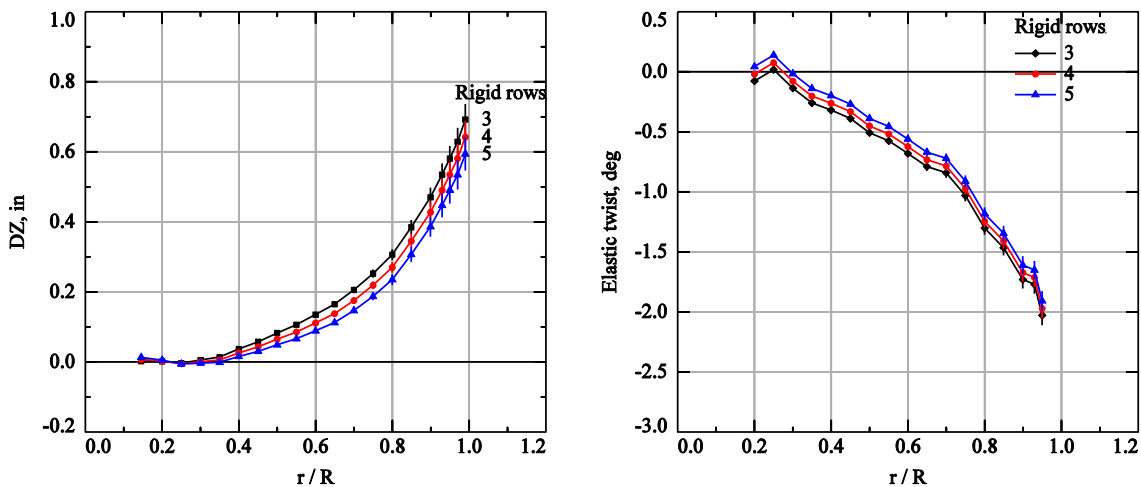


Figure 26. Effect of number of inboard rows of targets assumed to be rigidly connected (1250 RPM, $\theta_0 = 12^\circ$, blade SN002).

8.2.3 Effect of the number of rigid-body targets

An important source of uncertainty was the approximation that targets at inboard rows were rigidly connected. For baseline measurements, the first three rows ($r/R \leq 0.25$) of targets were assumed to be rigidly connected. Figure 26 shows the effect on bending and elastic twist of

expanding the set of rigid targets to the inboard four ($r/R \leq 0.30$) and five ($r/R \leq 0.35$) rows (1250 RPM, $\Theta_0 = 12^\circ$, blade SN002). The bending measurement at the tip decreased by about 0.1 inches and elastic twist became less negative by about 0.1° when the range of rigid targets was increased from three to five rows.

8.3 Lessons learned

In retrospect, there were several ways the photogrammetry measurements could have been improved.

First, it would have been instructive to investigate the poor repeatability of the blade deformation measurements by acquiring at least a few data points over longer time intervals (e.g., one minute). This would have allowed us to assess the apparent unsteadiness of the inflow and its effect on the blades.

Second, the alternate dropping of one count by the encoder unnecessarily complicated target finding and resulted in even and odd measurements that were offset from each other in azimuth by 0.35° . This was only a nuisance because the resulting jitter did not affect the blade deformation measurements.

Third, the orientation of the target board could have been aligned more accurately with the tunnel axes, especially the in-plane rotation (yaw). Better yaw alignment could have been accomplished using a laser level to sweep out a vertical plane aligned to the tunnel longitudinal axis. Misalignment of the target board shifted and rotated the space coordinates of the photogrammetry targets relative to true tunnel coordinates, but it did not affect the blade deformation measurements because the photogrammetry measurements (in misaligned tunnel coordinates) were always transformed to the blade coordinate system. Only pitch, flap, and lag measurements—the three rotations of this transformation—were affected.

Fourth, a better adhesive should have been used to avoid the loss of targets near the tips of the blades.

9. Database

As discussed earlier, the blade-deformation data will be included in the larger set of HVAB test data and shared openly on a NASA-sponsored web site. This section describes the data to be included as well as the detailed format of the data files to be provided. These descriptions will be most valuable when viewing the actual data files (not provided as part of this document).

9.1 Bending and elastic twist

The blade-deformation database consists of three Excel workbooks, one for each research run, in which bending and elastic twist measurements at all test points are tabulated. Each worksheet tabulates five repeat data points for a single blade at a single collective pitch angle. The average and standard deviation of 128 once-per-rev instances are shown for each data point. In addition, the average and standard deviation of the five measurements are shown in columns L and M, respectively. Bending measurements have been interpolated to the elastic axis. Columns are labelled according to the DAS data points during which the photogrammetry images were acquired. Each tab is labeled by the range of DAS points that the sheet includes. Each worksheet also includes plots of bending and elastic twist versus radial position for all five repeat points, and, on separate axes, the average of the five points. Error bars indicate \pm one standard deviation.

Every fifth worksheet compares average data for each of the four blades at a single collective pitch (i.e., an average of five repeated points tabulated in columns L and M on the previous four worksheets). Also plotted on separate axes are the average bending and elastic twist of all four blades versus radial station. Tabs for these blade-to-blade comparison are labeled “B-to-B xx deg”, where xx is the collective pitch.

Following the last “B-to-B” tab, there are four “SNX sweep” tabs that tabulate the average bending and elastic twist of blade X (X = 2, 3, 1, and 5) over the range of collective pitch angles.

Finally, the “Ave sweep” tab shows the average bending and elastic twist of all four blades over the range of collective pitch angles.

9.2 Pitch, flap, and lag

Pitch, flap, and lag measurements derived from the rigid-body targets are compared to measurements of the same quantities by the DAS in three Excel workbooks, one for each research run, and a fourth that distills data from all three runs. The first three tabs of the first three workbooks tabulate average pitch, flap, and lag measurements from the DAS and from photogrammetry (PG). In addition, for each blade, PG measurements at all collective pitch angles are plotted versus the corresponding DAS measurement, and the data have been fitted with a straight line: $PG = \text{slope} * DAS + \text{offset}$. The last four tabs of the workbooks tabulate only PG measurements. The data are staggered so that each column includes data for a single blade. Each PG measurement is the average of 128 consecutive once-per-rev measurements at azimuth = 270.

The fourth workbook includes plots from all three runs and tabulates, by blade and run number, the slope and offset of PG vs. DAS. The last tab (“All-in-one Table”) tabulates the slopes and offsets for all cases.

10. Concluding remarks

The deformations of all four blades of the HVAB rotor in hover were measured by stereo photogrammetry during the HVAB test campaign in the NFAC 80- by 120-ft Wind Tunnel. Measurements were made at three tip Mach numbers (0.60, 0.65, and 0.675) over a range of collective pitch set points between 4° and 14°. As expected, bending deflections increased as the collective pitch set point (and thrust) increased, and elastic twist became increasingly nose down. The short-term (cycle-to-cycle) and longer term (test-point-to-test-point) repeatability of the measurements was poor and varied deterministically, probably due to unsteady recirculation of air in the test section. To mitigate the effects of this unsteadiness, the measurement of each blade at each test condition was repeated five times, and the average of these repeat measurements was averaged over all four blades. The blade-deformation measurements were tabulated in Excel spreadsheets and are archived in the HVAB database.

11. References

1. Overmeyer, A.D., Copp, P.A., and Schaeffler, N.W., "Hover Validation and Acoustic Baseline Blade Set Definition," NASA TM 2020-5002153, May 2020.
2. Norman, T.R., Heineck, J.T., Schairer, E.T., Schaeffler, N.W., Wagner, L.V., Yamauchi, G.K., Overmeyer, A.D., and Ramasamy, M., "Fundamental Test of a Hovering Rotor: Comprehensive Measurements for CFD Validation," presented at the Vertical Flight Society's 79th Annual Forum & Technology Display, West Palm Beach, FL, May 16-18, 2023.
3. Brooks, J.D., and Beamish, J.K., "Measurement of Model Aeroelastic Deformations in the Wind Tunnel at Transonic Speeds Using Stereophotogrammetry," NASA TP 1010, 1977.
4. Abdel-Aziz, Y.I., and Karara, H.M., "Direct Linear Transformation from Comparator Coordinates into Object Space Coordinates in Close-Range Photogrammetry," presented at Close Range Photogrammetry Symposium, Urbana, IL, 1971.
5. Abrego, A.I., Meyn, L., Burner, A.W., and Barrows, D.A., "Summary of Full-Scale Blade Displacements of the UH-60A Airloads Rotor," presented at the AHS Technical Meeting on Aeromechanics Design for Vertical Lift, San Francisco, Jan. 20-22, 2016.
6. Schairer, E.T., Heineck, J.T., Spooner, H., and Overmeyer, A.D., "Blade Displacement Measurements of a Rotor in Forward Flight in the Langley 14- by 22-Foot Wind Tunnel," AIAA Paper 2021-0131, presented at SciTech 21 Forum, virtual event, Jan 2021.
7. Fulton, M.V., Gold, N.P., Nielsen, G.E., Mansur, M.M., Tischler, M.B., and Domzalski, D.B., "Development and Hover Testing of the Active Elevon Rotor," American Helicopter Society 68th Annual Forum Proceedings, Fort Worth, TX, May 2012.
8. <https://www.geodetic.com/v-stars/> (6-13-2023).
9. Fleming, G.A., "RASP:Rotor Azimuth Synchronization Program (RASP) User's Guide, Version 3.1," NASA Langley Research Center, Feb. 6, 2008.
10. Wolf, P.R., *Elements of Photogrammetry*, McGraw-Hill Book Company, New York, 1974.
11. Cattafesta, L.N., and Moore, J.G., "Review and Application of Non-Topographic Photogrammetry to Quantitative Flow Visualization,: Paper 96-2180 presented at 19th AIAA Advanced Measurement and Ground Testing Technology Conference, New Orleans, LA, June 17-20, 1996.
12. Liu, T., and Burner, A.W., "Photogrammetry Toolbox Reference Manual," NASA CR-2014-218518, Sept., 2014.
13. Zhang, Z., "Flexible Camera Calibration by Viewing a Plane from Unknown Orientations," presented at International Conference on Computer Vision, Corfu, Greece, Sept. 1999, pp. 666–673.
14. Press, W.H., Flannery, B.P., Teukolsky, S.A., and Vetterling, W.T., *Numerical Recipes, The Art of Scientific Computing*, Cambridge University Press, Cambridge, 1986, pp. 523-528.

12. Appendix

PITCH			
Slope PG vs DAS			
RPM	1250	1310	1160
SN002	1.0122	1.0036	1.0122
SN003	0.9893	1.0359	1.0022
SN001	0.9905	0.9916	0.9898
SN005	0.9858	0.9854	0.985
Offset PG vs DAS			
SN002	-0.2898	-0.2339	-0.3032
SN003	-0.033	0.2036	0.4128
SN001	-0.4001	-0.4067	-0.3893
SN005	-0.0079	-0.0056	-0.0122

FLAP			
Slope PG vs DAS			
RPM	1250	1310	1160
SN002	1.0428	1.0492	1.0553
SN003	1.067	1.0796	1.0934
SN001	0.9992	1.0494	1.069
SN005	1.0443	1.1114	1.1006
Offset PG vs DAS			
SN002	0.2667	0.2971	0.2731
SN003	0.3952	0.3336	0.3064
SN001	0.2133	0.1683	0.1817
SN005	0.2134	0.15	0.1323

LAG			
Slope PG vs DAS			
RPM	1250	1310	1160
SN002	1.2994	1.4779	1.3032
SN003	1.3798	1.5159	1.355
SN001	1.8329	1.9056	1.2689
SN005	1.2341	1.4496	1.2971
Offset PG vs DAS			
SN002	4.9981	3.9705	4.9682
SN003	4.5802	4.9639	5.7785
SN001	5.598	6.3563	4.9811
SN005	5.3872	4.394	5.2803

Table 1. Slopes and offsets of linear fits of PG vs. DAS measurements: pitch (top-left); flap (top-right); and lag (bottom-left).